Nano Express

ACCEPTED MANUSCRIPT • OPEN ACCESS

Development of defect-free thin film nanocomposite membranes for desalination using recycled PET and 2D nanomaterials

To cite this article before publication: Mantsopa Koena Zamisa *et al* 2026 *Nano Ex.* in press https://doi.org/10.1088/2632-959X/ae5077

Development of Defect-Free Thin Film Nanocomposite Membranes for Desalination Using Recycled PET and 2D Nanomaterials

Mantsopa Koena Zamisa [a]*, Suprakas Sinha Ray [b,c], Vincent Ojijo [b], Tumelo Seadira [a], Rotimi Sadiku [d], Neeraj Kumar [b,e] and Makungu Madirisha [f,g]

[a]*Department of Chemical and Materials Engineering, College of Science, Engineering and Technology, University of South Africa P. O Box 1710, Johannesburg, South Africa*

[b]*Centre for Nanostructures and Advanced Materials, DSI-CSIR Nanotechnology Innovation Centre, Council for Scientific and Industrial Research, Pretoria 0001, South Africa.*

[c]*Department of Chemical Sciences, University of Johannesburg, Doornfontein 2028, Johannesburg, South Africa.*

[d]*Division of Polymer Technology, Department of Chemical, Metallurgical and Materials Engineering & Institute of Nanoengineering Research, Tshwane University of Technology, South Africa*

[e]*School of Engineering, Newcastle University, NE1 7RU, United Kingdom*

[f]*Department of Civil Engineering, College of Science, Engineering and Technology, University of South Africa P. O Box 1710, Johannesburg, South Africa*

[g]*Chemistry Department, College of Natural and Applied Sciences, University of Dar es Salaam, P. O Box 35061, Dar es Salaam, Tanzania*

*Correspondence author Email: zamism@unisa.ac.za

Keywords: Electrospun Recycled Polyethylene Terephthalate; Graphene oxide (GO); molybdenum disulfide (MoS_2); Desalination; Water permeability; Thin Film Composite membrane.

Abstract: This study investigates the development and properties of the thin film nanocomposite (TFNC) desalination membranes based on electrospun recycled polyethylene terephthalate (rPET) substrate layers. However, achieving a defect-free thin film active layer onto the highly porous electrospun nanofibrous membranes (ENMs) remains challenging. The ENM was thus modified with graphene oxide/ molybdenum disulfide (GO/MoS_2) to develop the defect-free TFNC membrane. Graphene oxide (GO) nanosheets were intercalated with MoS_2 and crosslinked polymer connectors. These as-prepared laminate layers were deposited onto the rPET nanofibers to function as an interlayer or transition layer between the electrospun substrate and the thin film active layer. The resultant rPET-GO/MoS_2 membrane was assessed in terms of physicochemical properties and performance. The hydrophilicity was greatly enhanced by the GO/MoS_2 interlayer, from 120 ° to 67°. The XRD supplied the evidence of successful intercalation of MoS_2 within the GO sheets, thus resulting in the tightening of the interlayer space within the sheets of the GO-MoS_2 membranes, from 0.86 nm for GO to 0.79nm

for GO/MoS_2. The nanochannel spacing of the GO-MoS_2 membranes was thus capable of retaining the salt ions during desalination. The properties of the tailored membrane, therefore, highlight the potential of electrospun membranes and 2D nanomaterials in offering sustainable materials towards ensuring continuous and economical water supply in emerging water supply alternatives such as desalination.

1. Introduction

In the face of escalating global water scarcity and the relentless pursuit of sustainable purification methods, the quest for innovative and efficient water filtration technologies has become more critical than ever [1, 2]. Desalination membranes commonly employ a thin film nanocomposite (TFNC) architecture, where a dense polyamide active layer provides ion rejection while a porous support layer facilitates water permeability. Phase-inverted polyethersulfone (PES) substrates are traditionally used as supports; however, their dead-end pore structure limits water flux [3]. Electrospun nanofibrous membranes (ENMs) offer an attractive alternative due to their highly porous, interconnected pore networks that enhance water permeability compared to conventional phase-inverted substrates [4-7]. Electrospun Polysulfone (PS), along with other polymers such as polyacrylonitrile (PAN) [4, 5], polyvinylidene fluoride (PVDF) [6], Polyurethane (PU) [7], etc., are commonly used as ENM substrates in water treatment.

Polyethylene terephthalate (PET), a commonly discarded plastic, has recently gained attention as an ENM substrate owing to its electrospinnability, low cost, mechanical properties, and recyclability [8]. The use of recycled PET (rPET) addresses the dual challenge of plastic waste management and membrane material sourcing [9]. However, the successful application of rPET ENMs in TFNC membranes requires overcoming two key challenges: the inherent hydrophobicity of rPET and the difficulty of depositing a defect-free polyamide active layer onto the highly porous nanofibrous surface.

Graphene oxide (GO) has emerged as an effective interlayer material, forming ordered laminates with interlayer nanochannels that enable size-exclusion-based ion separation while permitting water molecule transport [12, 13]. The hydrophilic nature of GO also enhances surface wettability, facilitating subsequent polyamide deposition [4]. However, GO membranes suffer from swelling in aqueous environments due to weak van der Waals interactions between sheets, leading to unstable interlayer spacing and compromised separation performance [15-18]. Several attempts to overcome this challenge includes introduction of crosslinkers (e.g. hydrophilic polymers such as PVA, amines, etc.) to form stronger bonds between the GO sheets [23], the removal of oxygen rich functional groups by the reduction of GO, thereby making it less hydrophilic [24]. These methods, however, still limit the permeability of membranes usually applied in the water purification processes that are highly prone to low flux challenges, such as desalination.

Molybdenum disulfide (MoS_2), a two-dimensional nanomaterial, maintains stable interlayer spacing in aqueous environments through stronger van der Waals forces [28]. Unlike GO, MoS_2 exhibits hydrophobic character and resistance to swelling. However, MoS_2 alone forms defective membranes due to poor sheet stacking compared to flexible GO sheets [29]. Recent

studies demonstrate that intercalating MoS_2 within GO laminates combines the advantages of both materials: the GO provides continuous film formation while MoS_2 stabilizes the interlayer spacing and enhances water flux [28, 43, 45].

Most studies employing GO/MoS_2 interlayers have utilized phase-inverted commercial membranes (e.g., PES, cellulose acetate) as supports [28, 43]. These substrates offer smoother surfaces that facilitate nanosheet stacking. The application of GO/MoS_2 interlayers on highly porous ENM supports remains largely unexplored, primarily due to the challenge of achieving uniform coating on rough, fibrous surfaces.

This study addresses this gap by developing a TFNC membrane incorporating an electrospun rPET support modified with a GO/MoS_2 interlayer and crosslinked polyvinyl alcohol (PVA) connector, followed by interfacial polymerization of a polyamide active layer. The GO/MoS_2 interlayer serves dual functions: (1) enhancing the hydrophilicity and surface smoothness of the rPET substrate to enable defect-free polyamide deposition, and (2) providing stable nanochannels for ion rejection. The use of recycled PET contributes to sustainability while the GO/MoS_2 hybrid addresses the stability limitations of pure GO membranes. The innovation marks a leap forward in addressing two of the world's most pressing environmental issues: water scarcity and plastic waste. Through a detailed examination of the fabrication process, characterization, and performance evaluation of these modified membranes, we aim to underscore their potential to revolutionize water filtration and desalination, paving the way for more sustainable and efficient water treatment solutions.

2. Experimental section

2.1. Materials

The materials for this study, including recycled Polyethylene Terephthalate (rPET) and Graphene Oxide (GO) powder [30, 31], were sourced from earlier research conducted at the Centre for Nanostructures and Advanced Materials, within the Department of Science and Innovation, Council for Scientific and Industrial Research (DSI-CSIR), South Africa. Sodium molybdate dehydrate and thiourea, were procured from Merck, South Africa. The chemicals utilized throughout the experiments were of research quality and were used without further modification. The commercial membrane used in this study, for comparison with the prepared membranes, was a flat sheet polyethersulfone (PES) ultrafiltration (UF) substrate (Sterlitech Corporation, PES membrane, 100 kDa MWCO). It was chosen as a representative conventional phase-inversion support layer.

2.2 Synthesis of two-dimensional (2D) MoS_2

2D-MoS_2 was prepared by a hydrothermal route, with minor variation from the method by Kumar *et al [32]* (i.e., thiourea was used instead of sodium diethyldithiocarbamate trihydrate). In this method, 2.5 g of sodium molybdate dihydrate ($Na_2MoO_4 \cdot 2H_2O$) and ethylenediaminetetraacetic acid (EDTA) were mixed in 100 ml of deionized water and stirred for dissolution. In a separate beaker, thiourea (NH_2CSNH_2) was dissolved in 75 ml of deionized

water (DI H_2O) and slowly introduced to the earlier mixture. The obtained reaction mixture was allowed to mix for 30 min. Thereafter, it was transferred to the stainless-steel autoclave (Teflon-lined) for hydrothermal heating at 200 °C for 24 h. After completion of the reaction, the autoclave was allowed to cool down naturally to 25 °C, and the black precipitate was collected using centrifugation with water/ethanol for 15 minutes. Further, the black precipitate was dried in the oven at 75 °C for 15 h.

‘

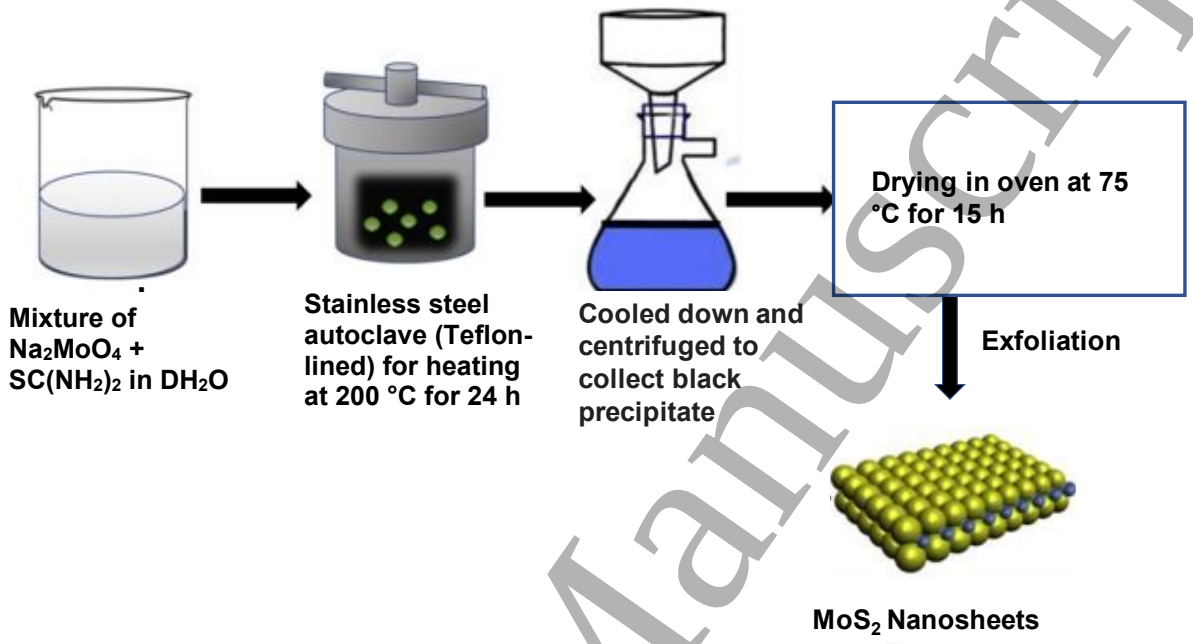

Figure 1. Schematic diagram showing the synthesis method for MoS_2.

2.3. Preparation of the rPET-GO/MoS_2

A mixture of GO and MoS_2 dispersions was prepared, and the resulting dispersion mixture was deposited or coated onto the previously prepared rPET ENMs as the substrate [33]. In brief, rPET pellets (2.5 g) were dissolved in a DCM/TFA solution mixture at a ratio of 3:7 and dissolved at room temperature for 24 hours. The resulting homogeneous polymer solution (at a concentration of 25 wt.%) was mixed with GO powder as a filler, at varying loads, to enhance the hydrophilicity of the resulting composite membrane. This was followed by electrospinning of the polymer solution under optimized parameters: 15 kV, 15 cm spinning distance, and 5 µL/min polymer solution flow rate. The resulting fibers were collected on a spinning drum, while the solvents evaporate, and thus collected as rPET ENMs [34]. For rPET ENMs modification, a fixed amount of GO (15 mg) adopted from our previous work [34], was used in combination with varying amounts of MoS_2 (1, 3, 5 mg), and dispersed in 50 mL H_2O. The resulting mixture (GO-MoS_2) was sonicated and used for coating rPET via the Vacuum Assisted Self-Assembly (VASA) Filtration technique (Figure **S1**). The resulting rPET-GO/MoS_2 composite membranes were labeled as rPET-GO/MoS_2-1, rPET-GO/MoS_2-3, and rPET-GO/MoS_2-5, for the 1, 3, and 5 mg added to the fixed amount of 15 mg GO, respectively.

Among the obtained membranes, rPET-GO/MoS_2-5 showed a promising coating compared to others and therefore was the selected membrane for further performance investigations.

2.4. Addition of cross-linked PVA to rPET-GO/MoS_2

The cross-linked polyvinyl alcohol (PVA) was added to rPET-GO/MoS_2-5, to function as a connector to the GO/ MoS_2 coating. Firstly, the PVA solution was prepared by the slow addition of PVA powder to the H_2O under continuous stirring at 500 rpm, for 2 hours at 90 °C, to fully dissolve the PVA and form a homogeneous PVA solution, as reported in the literature [35]. The prepared PVA solution (at varying concentrations of 0.05, 0.25, and 0.5 wt.%) was added to the GO/MoS_2-5 dispersion with continued stirring at the same stirring speed at 25 °C, to form a dilute homogeneous PVA/GO-MoS_2 solution mixture. The dilute PVA concentrations were selected to prevent membrane blockage due to the formation of a thick PVA layer. This was followed by the addition of cross-linker (Tetraethyl orthosilicate, TEOS) at dosages of 50µL, with a drop of 0.1M HCl (in ethanol). The solution was continuously stirred for 1 h to achieve proper crosslinking. The solution was then sonicated for 10 minutes, followed by coating onto rPET by the VASA method, and oven drying at 90 °C for 5 minutes. The membranes were referred to as rPET-GO/MoS_2/PVA0.05, rPET-GO/MoS_2/PVA0.25, and rPET-GO/MoS_2/PVA0.50, respectively.

The rPET substrate coating using the prepared solutions by the VASA method, is depicted in Figure **S1** in the Supporting Information. This was applied for the preparation of the three types of laminar membranes, namely, rPET-GO (from the previous work), rPET-GO/MoS_2, and rPET-GO/MoS_2/PVA. All prepared membranes were oven-dried at 90 °C for a short period of 5 minutes, to avoid overheating and membrane shrinkage.

2.5. Preparation of the polyamide active layer by the interfacial polymerization (IP) method

The previously prepared rPET substrate modified or coated with GO/MoS_2/PVA, can provide a suitable platform for the preparation of the polyamide (PA) active layer, due to the improved hydrophilicity and surface roughness. The IP process was carried out as previously reported [36]. In brief, 2% of m-phenylenediamine (MPD) was dissolved in DI water, while 0.15% of trimesoyl chloride (TMC) was dissolved in hexane. The rPET-GO/MoS_2/PVA0.50 membrane was the selected membrane and was used as a substrate for the deposition of the active layer. The substrate was first dipped into the MPD solution for 1 minute, followed by soaking in the TMC solution for 3 min to allow for the IP process to take place. The membrane was then placed in an oven at a temperature of 60 °C for 5 min for curing. Thereafter, it was stored under ambient conditions overnight to complete the curing process. The membranes were stored in DI water until further use. The sample was labeled rPET-GO/MoS_2/PVA/PA.

2.6. Characterization of rPET, GO, MoS_2 and rPET-GO/MoS_2

The investigation of the surface morphology of rPET, GO, MoS_2 and rPET-GO/MoS_2 with PVA and PA membranes employed scanning electron microscopy (SEM) (model JEOL JSM-7500F, Tokyo, Japan), with settings adjusted to an accelerating voltage of 3 kV and an emission current of 10 µA in a high vacuum environment (9.5×10^{-5} Torr). Before SEM imaging, the membrane samples were cut and then coated with carbon (the sputter coating was performed

in one cycle to avoid over-coating) to ensure conductivity under the electron beam. Additionally, the surface features (roughness and topography data) of rPET, GO, MoS_2, rPET-GO, and the rPET-GO/MoS_2 or rPET-GO/MoS_2/PVA/PA composite membranes were examined using Multimode Atomic Force Microscopy (AFM, NanoScope Version (R) IV, London, UK), which also measured the height, lateral dimensions, and thickness of the GO sheets. GO suspensions were spread onto silicon wafer substrates, left to air dry, and then placed on an AFM stage for assessment. The fiber diameters were determined using a freely available image analysis program (Image J software, https://imagej.nih.gov/ij/). About 100 individual fibers were measured per sample to obtain the mean fiber diameter.

Chemical functionalities within the rPET, GO, rPET-GO, rPET-GO/MoS_2, and rPET-GO/MoS_2/PVA/PA membranes were analyzed through Attenuated Total Reflectance Fourier Transform Infrared (ATR-FTIR) Spectroscopy using a Perkin-Elmer Spectrum 100 spectrometer, spanning a wavelength range from 800 to 4000 cm^{-1} with 32 scans at a resolution of 4 cm^{-1}. Furthermore, X-ray Diffraction (XRD) analysis, utilizing a PANalytical X'Pert PRO instrument (The Netherlands) and equipped with Cu Kα radiation (λ = 1.5406 Å), was conducted to assess the chemical and crystalline composition, specifically to identify crystalline phases and to calculate the interlayer spacing between nanosheets using the Bragg equation, as depicted in equation **1** [37]:

$$2d.sin\theta = n.\lambda \quad (1)$$

Where d is the interlayer spacing of GO and MoS_2 nanosheets (nm) in rPET-GO and rPET-GO/MoS_2 membranes, θ is the diffraction angle, n = 1 as the order of reflection, and λ = 1.540598 and is the wavelength of X-ray.

Hydrophilicity was assessed using a DSA100 contact angle analyzer from KRUSS, Germany, through water contact angle (WCA) measurements to evaluate the surface wettability of the rPET, GO, MoS_2 and rPET-GO/MoS_2 or rPET-GO/MoS_2-PVA-PA membranes. This was achieved by employing the sessile drop technique, where the membrane samples were positioned on a stage, and droplets ranging from 6 to 8 microliters (μL) of deionized water were precisely applied to the surface with a micro-syringe. A real-time camera recorded the droplet's profile, allowing for the calculation of the WCA.

The surface area of GO and MoS_2 was determined using the Brunauer-Emmett-Teller (BET) method on a Micromeritics TriStar II 3020 Version 3.02 instrument. Before analysis, the samples underwent degassing at 150 °C for 4 hours. Additionally, the thermal stability of rPET, GO, and rPET-GO/MoS_2 or rPET-GO/MoS_2-PVA was analyzed through Thermogravimetry Analysis (TGA), using a PerkinElmer TGA 4000, with a consistent heating rate of 10 °C/min in an air atmosphere, across a temperature spectrum from 25 to 800 °C.

2.7. Permeability testing of nanofibrous thin film nanocomposite membranes (rPET-Go/MoS_2-PVA/PA

The permeability and desalting properties of the composite rPET-Go/MoS_2/PVA/PA membranes were studied using a stainless steel dead-end RO filtration cell (Sterlitech HP4750 Stirred Cell, 300 mL) as shown in Figure **2** below. For the permeability test, DI water was used

as the feed to the filtration cell operating at 0 to 600 kPa from the nitrogen-compressed gas cylinder. The salt rejection tests were carried out using a 2000 ppm salt solution (20 g/L NaCℓ) as a feed. Filtrate was collected at varying pressures of between 0.2 and 600 kPa. The permeate flux was calculated by using the equation **2**:

$$J = \frac{Q}{P \times A \times T} \quad \textbf{(2)}$$

Where J is the water flux across the membrane ($L.m^{-2}.h^{-1}$), Q is the volume of the collected permeate water (L), P represents the operating pressure (bar), A is the effective area of the membrane (14.6 cm^2), and t is the permeation time (h). Salt rejection was also evaluated using the RO system. The salt feed solution was used with a stirrer inside the filtration cell to minimize the effects of internal concentration polarization (ICP) [38]. Conductivities of the feed (C_f) and the permeate (C_p) were measured for the calculation of rejection by using equation (3.3):

$$R\ (\%) = \left(1 - \frac{C_p}{C_f} \times 100\right) \quad \textbf{(3)}$$

where C_p and C_f are the concentrations of salt in the permeate and feed sides, respectively. The conductivity of the feed and permeate solutions was measured using a conductivity/TDS portable meter (Hanna Instruments HI-8033, UK).

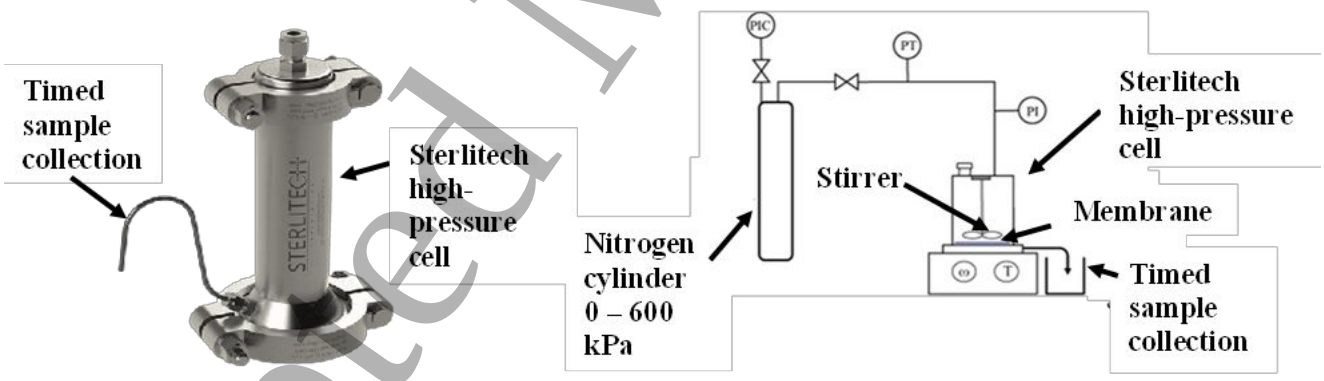

Figure 2. Dead-end RO filtration set used for permeability and rejection studies.

3. Results and Discussions

3.1. Morphology of the synthesized nanomaterials

The topographic morphology of the synthesized GO and MoS_2 powders is shown in the SEM images in Figure **S2a & b** (Supporting Information). Simple synthesis methods were used to prepare the nanosheets. The GO was prepared by a low-cost, environmentally benign Hummer's method, while a 1-step and low-temperature hydrothermal method was used for the MoS_2. The nanoscale morphologies showed that the MoS_2 particles were a hierarchical

microsphere that consisted of several ultrathin MoS_2 sheets. Figures **S2a & b** show the powders of GO and MoS_2 in their aggregated form before sonication.

The BET surface area and curves of the GO and MoS_2 powders were obtained from the nitrogen adsorption-desorption isotherms displayed in Figure **S2c**, Supporting Information, showing a nonporous structure of the materials and following type IV isotherms with the hysteresis loops of type H3 for the GO and type H4 for the MoS_2 [39]. The surface area of GO was measured to be 15 m^2/g and is greater than that of MoS_2 (2.4 m^2/g). The measured surface areas were lower than those reported in the literature (>70 m^2/g), due to the agglomerates of the synthesized powders. This shows the need for sonication before use.

3.2. Construction of GO/MoS_2 (Intercalation of GO by MoS_2)

3.2.1. Surface properties of rPET-GO/MoS_2 membranes

The fundamental issue for GO membranes is the control of the interlayer spacing to make it an effective ion separation membrane layer to enhance its ion sieving effect [12, 40]. The increased GO dispersion volume leads to easier stacking of the GO sheets during vacuum filtration, to form an even and intact GO film without agglomeration [41, 42]. Using the same volume, MoS_2 (at various loadings) was mixed with the GO to form the MoS_2 intercalated GO sheets. At lower MoS_2 loadings (1 and 3 mg, i.e., rPET-GO/MoS_2-1 and rPET-GO/MoS_2-2, respectively), MoS_2 agglomerated on the GO surface, as shown by the arrows in Figure **3b.** The blue arrows show the clustered features with a morphology characteristic of agglomerated MoS_2 nanoflowers. Based on the contrasted morphology with the smooth GO film in Figure **4a**, these features are attributed to poorly dispersed MoS_2 agglomerates. MoS_2 clusters that did not intercalate into the GO sheets. The poor coating is also depicted in the photograph in Figure **3c**.

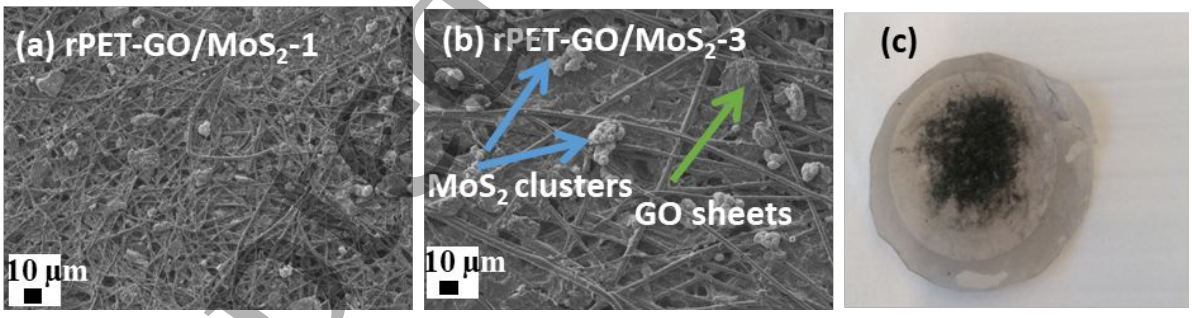

Figure 3. SEM images of the loosely bound GO-MoS_2 particles coated onto the rPET substrate at lower MoS_2 contents of 1 and 3 mg, respectively.

On the other hand, the higher MoS_2 content of 5 mg (rPET-GO/MoS_2-5) showed a rather uniform coating film, allowing MoS_2 to be intercalated or remain intact within the GO sheets **(**Figure **4b)**. The robustness of the membrane is, therefore, based on the quality of the coating in terms of achieving a GO film layer coating with the intercalation of MoS_2. The rPET-GO/MoS_2-5 was, therefore, the optimum membrane and the selected membrane for further

studies and labelled as rPET-GO/MoS_2. When compared to the black GO coating of the rPET-GO membranes in Figures **4a** and **a'**, the surface of the rPET-GO/MoS_2 membrane was relatively rougher and greyish, as observed in Figure **4 b.** This was confirmed by the AFM results in Table **1** below, thus indicating a successful intercalation of MoS_2. Compared to the smooth surfaces of the rPET-GO-coated membranes (although with the appearance of small wrinkles due to the thin flexible nature of the 2D GO sheets), the MoS_2-incorporated membrane surfaces presented a rougher surface, as shown in the figures**,** due to the intercalated MoS_2 causing the GO wrinkles to become rough [43]. Intercalated MoS_2 can thus offer stability to the GO sheets or act as nanochannels within the GO sheets, to facilitate selective ion transport, making the composite membrane suitable for enhanced permeability and desalination process. GO interlayer intercalation by nanomaterials such as 2D nanosheets has proven to create nanofluidic heterostructure channels in GO membranes [44, 45]. The three-dimensional AFM images in Figure **5** show the surface morphology of the coated membranes, and the visible nodes on the GO-MoS_2 membranes are due to the intercalated MoS_2 within the GO sheets. The disruption of film formation at low MoS_2 loadings (1, 3 mg) is a crucial point. We hypothesize that at sub-optimal concentrations, MoS_2 nanoflakes act as disruptive fillers rather than effective intercalants. They may create local defects and heterogeneities in the GO laminate, preventing the formation of a continuous, vacuum-filtered film. At the critical loading of 5 mg, there is likely sufficient MoS_2 to uniformly intercalate and bridge GO sheets, forming a cohesive hybrid network. In addition, for future studies, there will be an attempt to synthesize MoS_2 in the presence of GO to promote more intimate mixing and covalent bonding, potentially leading to even better film formation and stability.

The concentration of 5 mg MoS_2 was sufficient to form intercalated and intact structures within GO sheets, as opposed to the lower concentrations in Figure **3**, and therefore, was used for further studies.

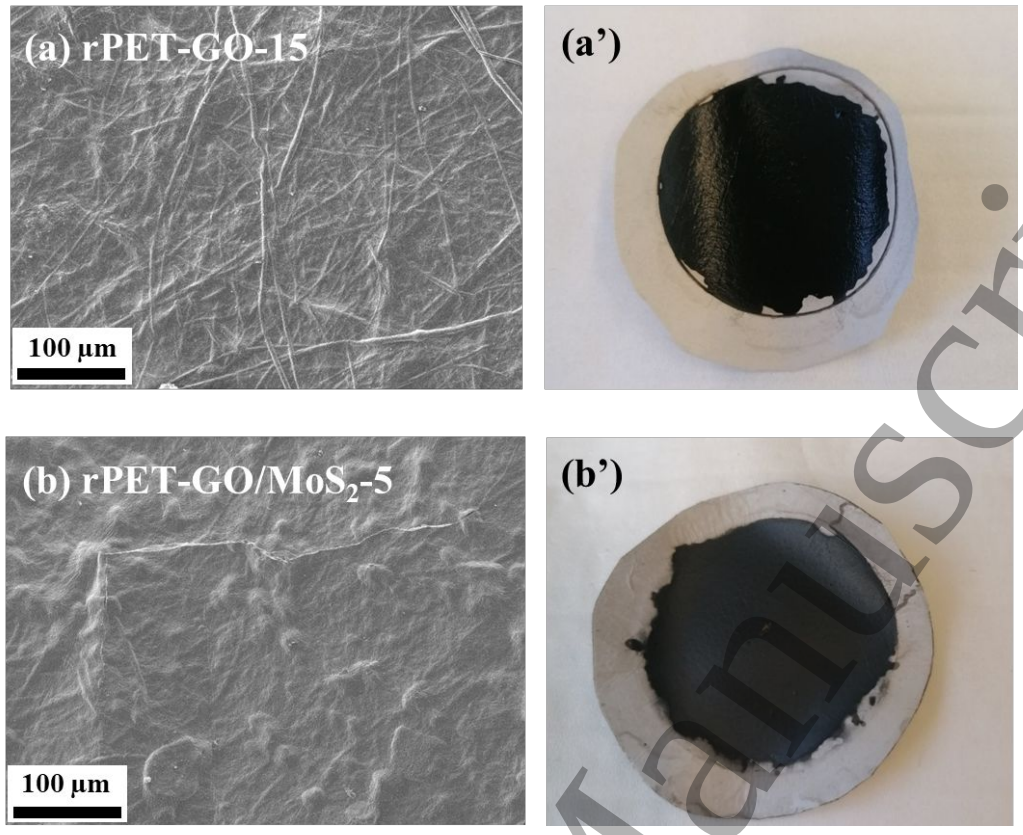

Figure 4. SEM images showing the morphology of the GO and MoS_2 coated rPET substrates: a) rPET-GO-10, b) rPET-GO/MoS_2-5. Digital photographs are shown in a') and b').

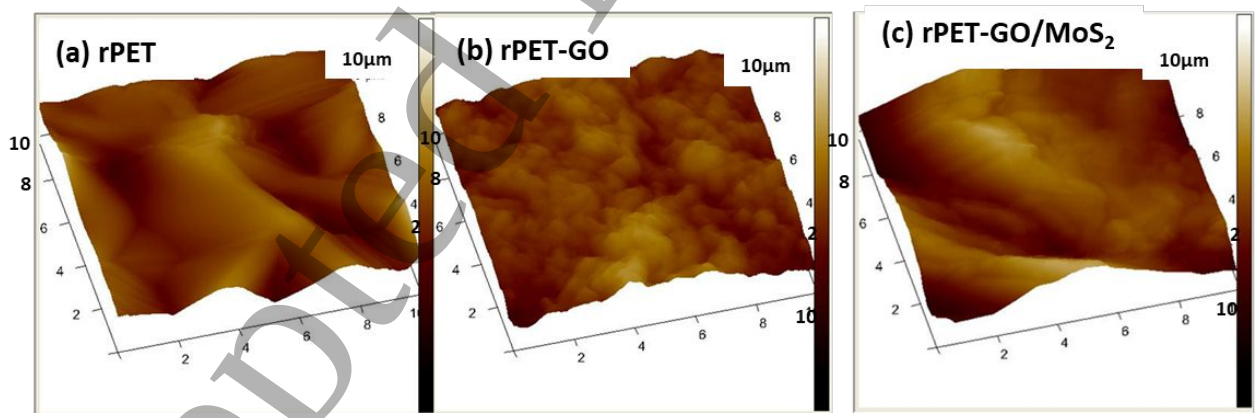

Figure 5. AFM micrographs of a) rPET, b) rPET-GO, and rPET-GO/MoS_2.

Table 1. Surface roughness parameters of rPET before surface coating (pristine and GO-loaded) and GO and GO-MoS_2 surface-coated membranes.

Membrane	Rq (nm)	Ra (nm)	R_{max} (nm)
rPET (pristine)	574	484	2838
rPET/GO (rPET)	317	194	3022
rPET-GO	80.8	63.1	603
rPET-GO/MoS_2	230	182	1449

Rq = root mean square average of height deviations; Ra = average roughness; R_{max} = the maximum distance between the highest point and the lowest point on the 3-D image profiles.

Figure **6a** shows the detectable MoS_2 diffraction peaks at 2θ 14.09°, 33.09°, 39.47°, 49.86, and 58.83°, corresponding to the planes (002), (101), (103), (105), and (110) of the hexagonal structure of the MoS_2 crystals. This shows that the MoS_2 nanosheets were successfully synthesized with good crystallinity [45]. The sharp intensive peak at 2θ = 14.09 °, corresponding to (002) indicates a tighter interlayer of MoS_2 (0.63 nm) than that of GO (0.86) nm. For the rPET-GO/MoS_2 membrane, the two visible peaks show that both the GO and MoS_2 peaks are evident (at 2θ of 11.14 ° and 13.85°, respectively). In addition, tighter interlayer spacing indicates that there was a uniform coating for the GO and MoS_2 coating or laminar layers that formed on the rPET surface. The compactness of rPET-GO/MoS_2 confirms the strong van der Waals force interaction between the GO and MoS_2 [45]. Therefore, the addition of MoS_2 to GO will ensure a weaker interaction between the MoS_2 and the H_2O molecules (due to the absence of hydrophilic groups on the MoS_2, as indicated by the WCA values in Table **2**, thereby enhancing the stability of the GO in water during filtration process [45].

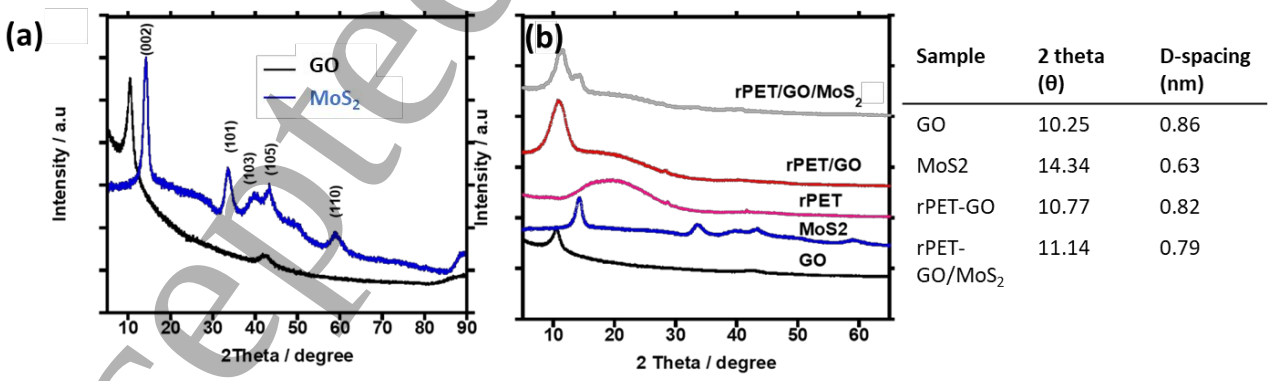

Sample	2 theta (θ)	D-spacing (nm)
GO	10.25	0.86
MoS2	14.34	0.63
rPET-GO	10.77	0.82
rPET-GO/MoS_2	11.14	0.79

Figure 6. XRD patterns of a) GO and b) MoS_2 powders, GO-coated and GO-MoS_2-coated rPET substrates.

The FTIR was used to study the surface chemistry of the GO and MoS_2-coated rPET substrates (Figure **7**). The spectrum of GO showed absorption peaks at 1048, 1410-1600, 1617, and 1742 cm^{-1} corresponding to the stretching vibrations of C—O alkoxy groups, C—O—C stretching of the epoxides and ethers, deformation of the –OH groups, the trapped H_2O molecules accompanied with the sp^2-hybridized carbon that remained after the oxidation reaction, and the carboxyl or carbonyl C=O group, respectively. epoxy, hydroxyl, and carboxyl groups, respectively. In addition, a broad and intense peak was observed between 3688-3040 cm^{-1} corresponding to the stretching of O—H bonds, to indicate the presence of abundant GO hydroxyl groups, and this broad GO peak, although less intense, was also observed in the rPET-GO and rPET-GO/MoS_2 membranes, to indicate the presence of the hydroxyl groups contributing to the hydrophilicity of the membranes. These were consistent with the previously shown XRD plots above, for rPET-GO/MoS_2 membranes, which clearly showed the GO and MoS_2 peaks. The absence of characteristic peaks of MoS_2 indicates that there was no chemical interaction with the MoS_2 planes [46]. The chemically stable MoS_2, therefore, did not affect the chemical structure of the rPET membrane.

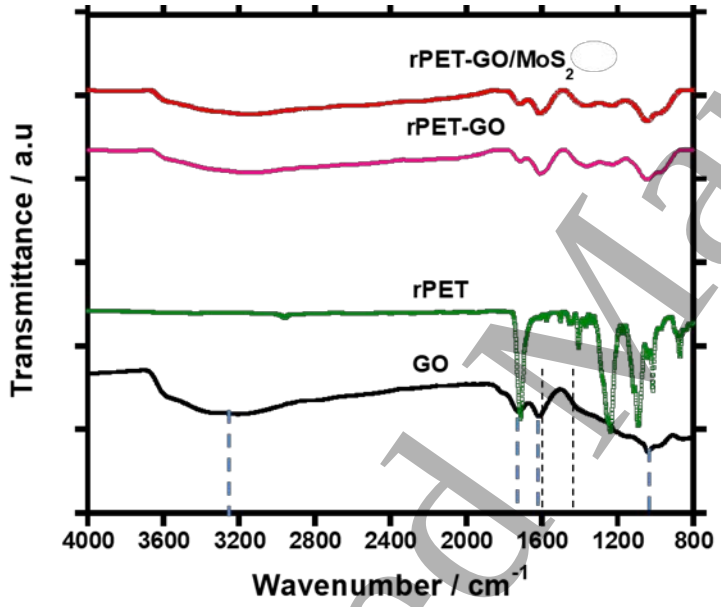

Figure 7. FTIR spectra of rPET substrate coated with GO (rPET-GO) and GO/MoS_2 (rPET-GO/MoS_2).

3.2.2. Incorporation of PVA into the GO-MoS_2 coating (interlayer) and the effect on the active layer formation

The addition or inclusion of crosslinked PVA (at various PVA concentrations of 0.05, 0.25, and 0.5%) to the GO/MoS_2 coating was to enhance adhesion between the GO/MoS_2 interlayer and the rPET substrate. Figure **8** shows the SEM images of PVA incorporated into the previously optimized GO/MoS_2-5 interlayer at various magnifications. The smooth defect-free coating of the previously coated GO and GO-MoS_2 substrates was maintained, and thus, the rPET substrate fibers were completely covered by the coating layer. During the VASA coating process, it is worth noting that the polymer penetrated the GO interlayers and the rPET pores or membrane pores under the vacuum. Once the GO stacking process was initiated, the PVA

started depositing onto the GO and between the GO laminate layers intercalated by the MoS_2. This formed the crosslinked polymer network and intercalated GO network. By so doing, the adhesion strength between the GO-MoS_2 interlayer and the rPET substrate was thus ensured [41]. The PVA formed a stable binding (as an anchor) between the GO-MoS_2 interlayer and the rPET substrate, as well as between the GO nanosheets. The TEOS cross-linker to the PVA polymer was also used to form a bond between the GO sheets. A similar observation was also noted in previous studies [47, 48]. In addition, TEOS was also used as a cross-linker to form a robust siloxane network, aiming to covalently anchor the PVA to GO functional groups and enhance the mechanical integrity and swelling resistance of the interlayer. The robustness of the membrane can therefore be afforded by covalent linkages between PVA and GO through TEOS crosslinking. This covalent linkage was assisted with the use of an acid and mild temperature conditions provided during sonication. The linkage was through the bonds formed between the silanol (Si—OH), –OH, and the –COOH groups of GO and PVA. The interaction of these materials is illustrated in Scheme **1**.

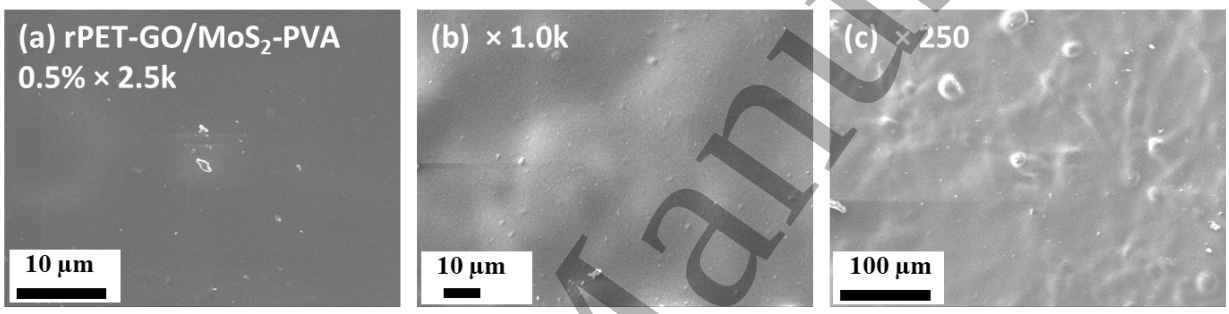

Figure 8. SEM images showing 0.5% PVA incorporated into the GO-MoS_2 coated rPET substrate (rPET-GO/MoS_2), as observed at magnifications of a) x2500, b) x1000 and c) x250.

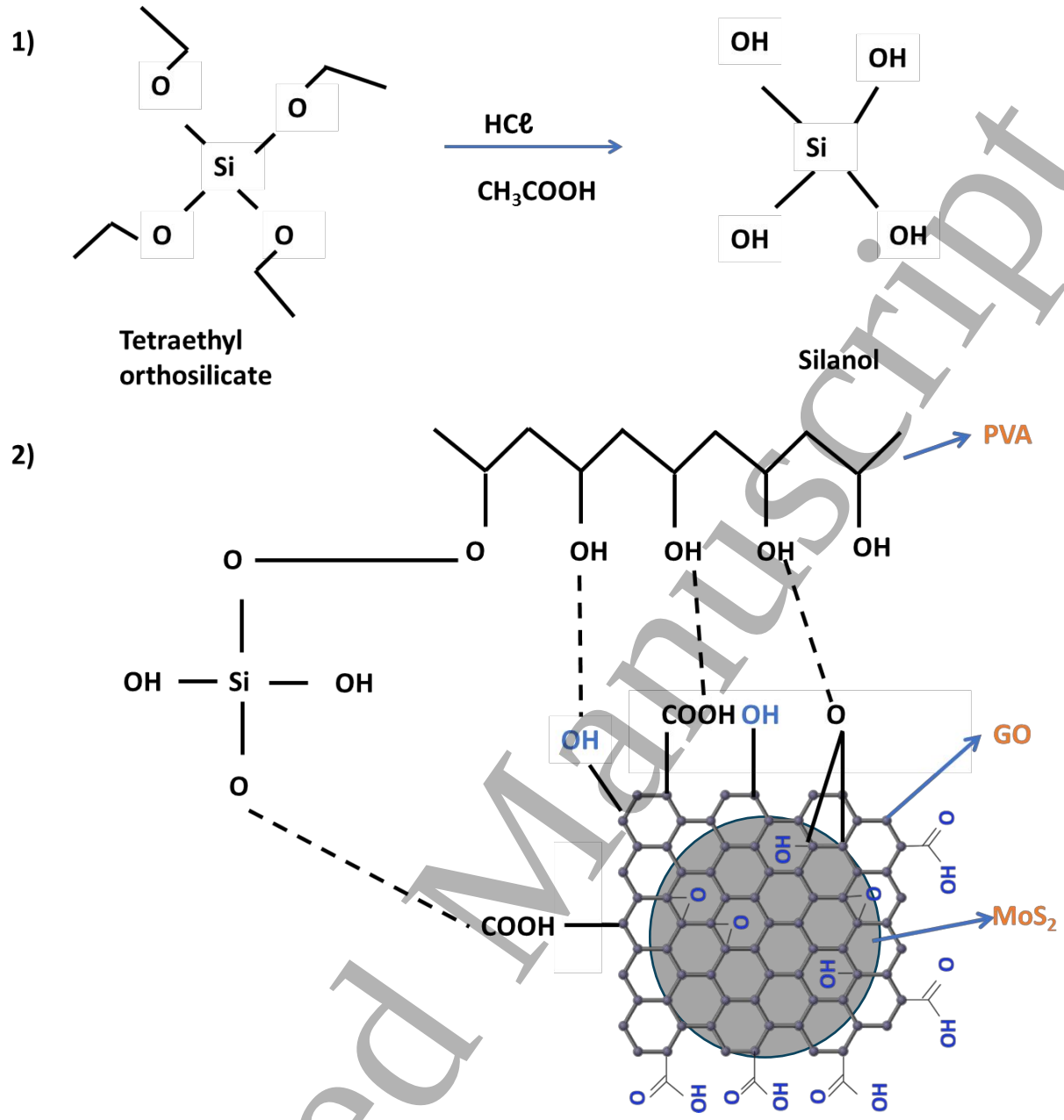

Scheme 1. Possible reactions of the PVA incorporated into GO-MoS_2 coated rPET (rPET-GO/MoS_2). Step 1) Conversion of TEOS to Si—OH, with HCℓ as a catalyst, and step 2) the interaction between GO and silanol.

Following the addition of crosslinked PVA to the rPET-GO/MoS_2, the polyamide (PA) thin film active layer was coated as the thin film nonporous top layer to the rPET-GO/MoS_2-PVA, through the IP process. Figure **9** shows the highly porous rPET substrates, before (Figure **9a**) and after (Figure **9b, c**) coating with the PA active layer. In Figure **9b**, the PA active layer is deposited directly onto the unmodified rPET substrate, i.e., without the inclusion of the GO/MoS_2 interlayer. Therefore, this led to ineffective coating of the PA layer, as the rPET was partially coated and the uncoated nanofibers (particularly the top section of the substrate) were

protruding and still clearly visible. The reason is that the monomer solutions penetrated through the highly porous rPET substrate during the IP procedure rather than being retained on the surface. Due to the absence of an interlayer, the surface features of the rPET substrate, such as the pore size, roughness, and hydrophilicity, are the key factors contributing to the success of the IP process during PA thin film layer formation onto a substrate [49], which were not improved, thus leading to poor facilitation of the PA deposition onto the rPET substrate. This led to uneven, thin-film active layer formation, thus leading to the development of defects within the resulting PA layer. The defective active layer is the reason for the poor desalination performance (in terms of salt rejection) of ENM-based TFNC membranes [50]. On the other hand, the presence of the GO/MoS_2 interlayer led to the successful PA layer deposition onto the rPET-GO/MoS_2-PVA. The interlayer facilitated the deposition and formation of the PA layer by providing a smooth, less porous, and hydrophilic surface. The rough ridge-and-valley morphology was typical of PA layers seen on all the PA-coated membranes [36]. The pore structure of the membranes was quantitatively assessed from SEM micrographs using ImageJ software. The pristine electrospun rPET substrate exhibited an average fiber diameter of 450 ± 120 nm and a mean surface pore size of 1.8 ± 0.6 μm, characteristic of the highly porous ENM structure. Following VASA deposition of the GO/MoS_2 interlayer, the surface pores were substantially reduced, as the GO laminates forming a continuous coverage over the underlying nanofibers. This pore size reduction is critical for preventing monomer penetration during IP and facilitating defect-free PA layer formation. After incorporation of crosslinked PVA and subsequent PA deposition via IP, the membranes transform to nonporous, indicating complete coverage by the dense active layer.

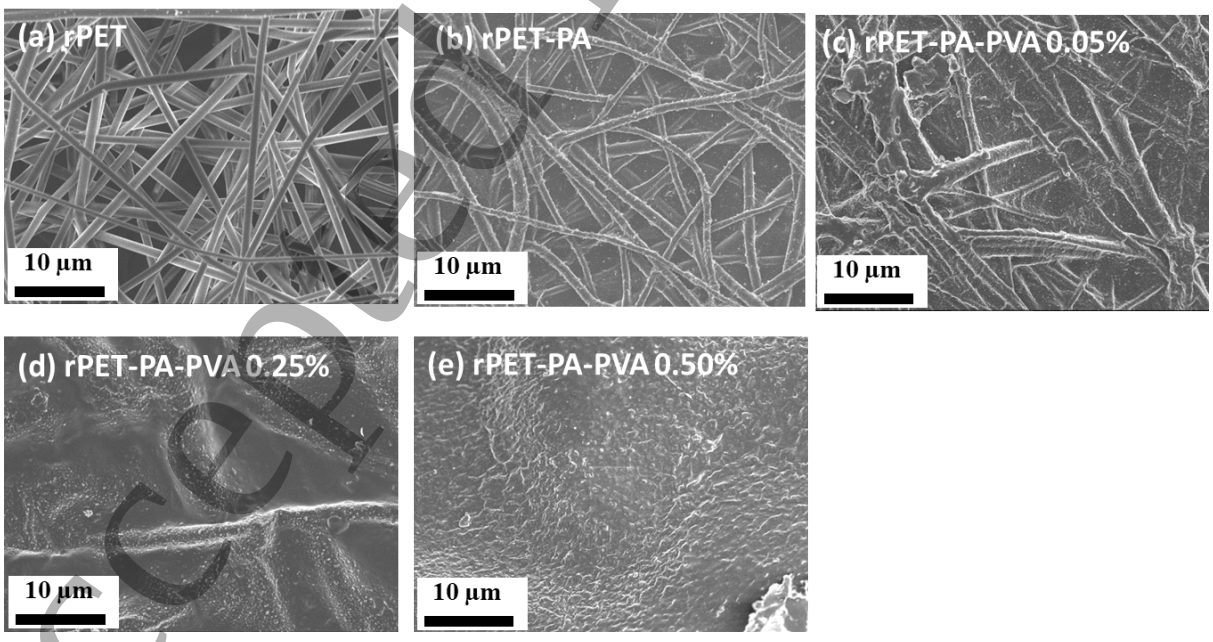

Figure 9. SEM images showing a) rPET substrate (without the GO/MoS_2 interlayer and before PA layer deposition, b) PA layer deposited onto unmodified rPET (rPET-PA), c-e) PA

layer deposited onto the rPET-GO/MoS_2 coated rPET with PVA at various concentrations of c) 0.05, d) 0.25 and e) 0.5%.

Thermal analysis was conducted to determine the decomposition and thermal stability of materials. Figure **10** illustrates the TGA and the DTG curves of GO and the GO/MoS_2-coated membranes with the inclusion of PVA as a binder to the GO nanosheets. Based on the TGA derivative curves in Figure **10b**, the GO powder undergoes 3 stages of mass loss, namely: H_2O loss or dehydration, thermal degradation of the oxygen functionalities, and carbon combustion, respectively [31]. The initial weight loss at 28 °C, signifies the onset loss due to the evaporation of H_2O. The main weight loss due to evaporation occurred at 57.19 °C. During the 2nd stage, the onset degradation at 140 °C was due to the loss of surface oxygen-containing functional groups from the GO basal planes, hydroxyl groups decompose around 200 °C. The major weight loss of these functional groups occurred at 195.49 °C. This is accompanied by the release of CO, CO_2 gases, H_2O moisture release, and decomposition of the carboxylic group [51, 52]. Finally, stage 3 is the region of degradation for GO, which was therefore between 140 and 302.5 °C. About 19% of GO remained after the TGA measurement at 900 °C. When compared to the GO, PVA undergoes a two-step degradation (at 57.19 and 195.49 °C) and (48 and 318 °C), while the rPET undergoes a single-step degradation at 439.43 °C. For rPET, degradation took place between 349.43 and 494.14 °C, with minor weight loss due to evaporation of H_2O between 81.07 and 107.2 °C. The onset degradation was observed at 349.43 °C (onset temperature) and the main degradation at 439.22 °C (peak degradation temperature). The onset temperature and peak degradation temperatures were almost similar to those of the PET reported in the literature [53]. The initial weight loss for the 0.5% PVA was observed at 102.39 °C. The onset of degradation starts at 225.03 °C. Two major degradation zones: the first one observed between 225 – 373 °C, with the peak degradation at 324.35 °C. The second degradation zone was between 225 – 543 °C, with the degradation peaking at 434.45 °C. Two degradation steps were obtained for 0.25% concentration at 156 and 433 °C, and only one step for 0.05% concentration at 433.91 °C. For the 0.25% sample, the initial weight loss was observed at 151.05 °C, and the onset degradation started at 262.9 °C. The degradation region for this sample was at 262.9 – 492.64 °C, with the major degradation peaking at 434.45 °C. The 0.05% sample had a negligible loss between 97.41 – 181.7 °C, followed by an onset of degradation at 275.44 °C. The minor loss due to degradation was around 336.89 °C, while the main degradation zone was observed at 434.45 °C.

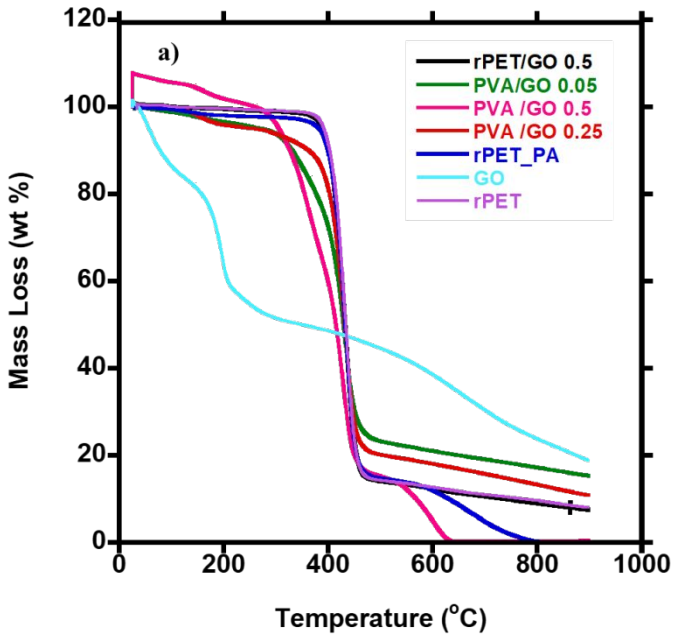

Figure 10. TGA curves of rPET-GO-MoS_2 membranes with the addition of PVA as a nanosheet connector at various concentrations of 0.05, 0.25, and 0.5% with a PA layer.

In general, higher roughness in hydrophilic membranes results in lower WCA. For hydrophobic membranes, on the contrary, higher roughness results in higher WCA [54]. The wettability or hydrophilicity of the substrates is characterized by measuring the WCA on the membrane surface. As shown in Table **2**, the water contact angles of all the membranes, besides the uncoated rPET substrate, were below 90°. The synthesized MoS_2 in the current study was hydrophobic, unlike the other commercially available hydrophilic MoS_2 in literature (which reduces the WCA to 30° [46]. The hydrophobicity of the GO-MoS_2 should therefore contribute towards the GO stability [43]. However, the rPET-GO/MoS_2 displayed the same hydrophilicity as the rPET-GO. This could be attributed to the intercalation of the MoS_2 sheets within the GO sheets, thereby implying that the GO sheets were on the upper surface while the MoS_2 was embedded due to intercalation, while maintaining the surface roughness of the MoS_2 agglomerates, as shown by the AFM results in Table **1**. Coating of the PA active layer onto the rPET-GO/MoS_2-PVA resulted in a hydrophilicity of 67°, which was typical of the PA layer. The hydrophilicity in reverse osmosis/nanofiltration (RO/NF) TFNC membranes is beneficial for membrane permeability (by enhanced attraction of water molecules towards the membrane nanochannels) and mitigates fouling (by weakening the attachment of contaminants onto the membrane surface) [55].

Table 2. Hydrophilicity of Membranes.

Membranes	**WCA (°)**
rPET	120 ± 28
rPET-PA	110.11 ± 23
rPET-GO	93.38 ± 7
rPET- GO/MoS_2-5	93.38 ± 38
rPET-GO/MoS_2-PVA-0.05%	79.84 ± 11
rPET- GO/MoS_2-PVA-0.25%	74.94 ± 6
rPET- GO/MoS_2-PVA-0.50%	67.31 ± 5

3.3. Membrane permeability and separation (salt rejection) performance

The desalination performance of the rPET-GO/MoS_2-PVA-PA membrane (labelled as rPET-GO/MoS_2), was tested with the low-pressure (0-600kPa) dead-end RO system. Before running, the membrane was first compacted under the maximum pressure for 1 hour, for stabilization. The results are presented in Figure **11**. For pure water permeability or flux measurements, DI water was used as the feed to the filtration cell, while 2000 ppm NaCl solution was used as the feed solution, for the salt rejection measurements. The tightly packed and intact GO and GO/MoS_2 coatings possess active layer features in the sense that the compact nanochannels provided by the GO sheets can reject contaminants (ions), as shown by the *d*-spacing in the previous sections while the water molecules permeate through the porous rPET substrate. The separation mechanism through such membranes was, therefore, expected to be size exclusion and electrostatic interactions between the negatively charged rPET-GO/MoS_2 membrane surface and the positive ions [56].

As the primary control of the d-spacing was the MoS_2 loading, which directly reduced the GO d-spacing from 0.86 nm to 0.79 nm as shown by the XRD data. The TEOS cross-linked PVA network likely further restricts dynamic swelling. By adjusting parameters such as larger organic cations as spacers, varying the oxidation degree of GO, or using different 2D materials, the interlayer spacing could be precisely engineered to target various ions (e.g., divalent Ca^{2+}, Mg^{2+} or small organics).

Similarly, coating the PA active layer directly onto an unmodified rPET substrate (rPET-PA) (i.e. without the hydrophilic GO or GO/MoS_2 interlayers) led to the formation of a defective PA active layer. The PA layer was, therefore, not evenly coated onto the highly porous and hydrophobic rPET substrate. Rather than forming an even continuous layer onto the rPET, the monomers for PA penetrated through the highly porous hydrophobic rPET fiber substrate, as previously shown by the uneven coating in Figure **9b**. The hydrophobic rPET fibers were partially covered by the PA layer and still visibly showing on the surface rather than having a complete coverage that results in a smooth even coating. This was also indicated by the

hydrophobicity of the rPET-PA with a WCA of 110.11°. The surface modification by the GO coating decreased the WCA of the rPET substrate from 120 to 93°, thus indicating the effectiveness of the GO interlayer in enhancing the hydrophilicity of the rPET substrate. Previous reports have also shown similar enhancement in hydrophilicity (i.e., 22%) by the GO interlayer [57]. In addition, the similarities in the WCA values for both rPET-GO and rPET-GO/MoS_2 coated membranes may imply that the GO sheets are on the membrane surface, while most of the MoS_2 is embedded or intercalated within the GO sheets. The addition of PVA connector to the nanosheets enhanced the hydrophilicity of the rPET-GO/MoS_2 from 93 to 67°, and this hydrophilicity improved with PVA content from 79 to 67° with an addition of 0.05 to 0.5% PVA, respectively.

The salt rejection and permeability were tested under varying pressures of between 2 to 6 bars. Both the permeability and salt rejection increased with an increase in pressures of up to 6 bars, at all-time intervals of 5 – 20 min. This explains the high-water permeability of the fabricated rPET-GO/MoS_2 membrane as compared to the commercial membrane **(**Figure **11b)**. As the filtration cell used was only operating at low pressures, low fluxes, and salt rejections were achieved. Under the relatively low pressures used (≤6 bars), the pressure had no significant effect on the d-spacing, due to the significant elastic compression of the covalently cross-linked GO/MoS_2/PVA network. However, at much higher pressures typical of RO, this could become a factor. Future work should investigate this using in-situ characterization techniques. Had higher pressures (of around 15 bars) been used, much higher fluxes could have been achieved. However, due to the low thickness of the prepared ENMs, they could have ruptured under high pressures. It is worth noting that the initial flux declined and this is common and often attributed to membrane compaction and the establishment of a steady-state concentration polarization layer in the dead-end cell, while our short-term tests show stable performance after this initial period. In addition, long-term stability tests (e.g., over 24-48 hours) under crossflow conditions are necessary for industrial considerations.

Table 3 highlights the comparisons of the current membrane with those in literature.

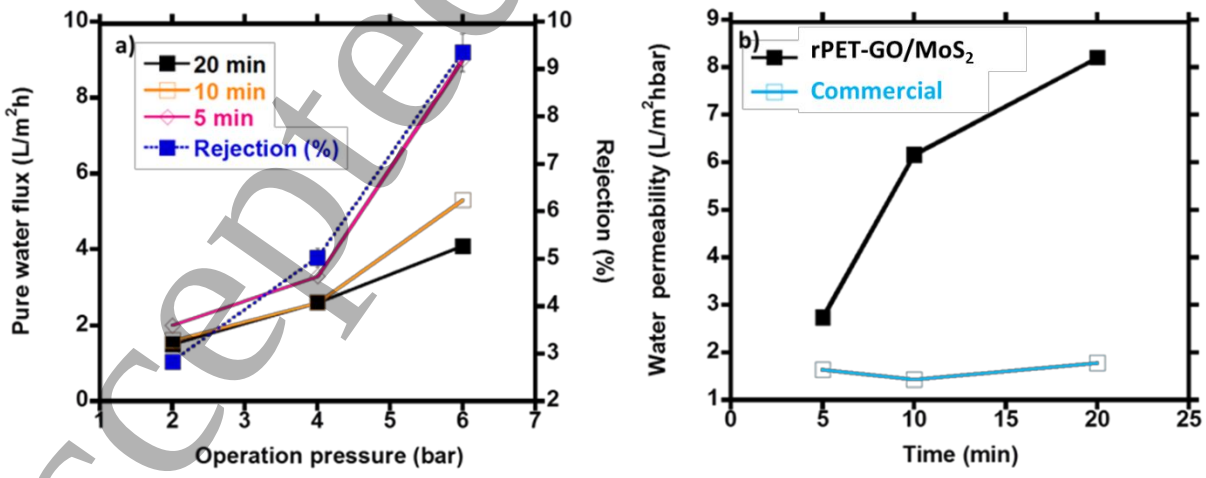

Figure 11. Separation or filtration properties of membranes a) water flux versus pressure and b) Water permeability over time, for the prepared rPET-GO/MoS_2 membranes versus the commercial PES substrate (a flat sheet PES UF substrate (Sterlitech Corporation, PES

membrane, 100 kDa MWCO), chosen as a representative conventional phase-inversion support layer).

In summary, the GO was successfully coated onto the porous rPET substrate and functioned as an interlayer with good surface wettability and smoothness. MoS_2 was successfully synthesized and incorporated into the GO interlayer and intercalated within the GO vacuum-stacked sheets for stability and good ion sieving ability of the tighter nanochannels offered, in addition to the surface charges provided by the functional groups of the GO. These tight nanochannels can thus offer good selectivity for the salt ions rejected via size exclusion. The hydrated Na^+ and Cl^- ions with sizes of 0.72 and 0.66 nm, respectively, the obtained nanochannel spacing of the rPET-GO/MoS_2 membranes, which was as low as 0.64 nm, was thus capable of retaining the salt ions. Characterization techniques such as Fourier Transform Infrared Spectroscopy (FTIR), Scanning Electron Microscopy (SEM), and contact angle measurements were employed to elucidate the morphological and chemical properties of the rPET-GO-MoS_2 membranes. These analyses confirmed the successful integration of the nanomaterials and revealed the formation of nano-channels on the surface of the rPET nanofiber network, attributed to the presence of the GO-MoS_2 interlayer. The modified rPET substrate can thus offer properties like those of conventional UF substrate layers but with the added nanochannels for enhanced permeability and salt rejection capability. This overcomes the low permeability challenges faced with the current TFNC membranes that make use of the less porous substrates prepared by the phase inversion method.

Table 3. Performance comparison with literature membranes

Membrane type	**Interlayer/nanomaterials**	**Crosslinker**	**Flux or permeability**	**Salt rejection**	**Ref.**
ENM: rPET TFNC	GO/MoS_2	PVA/TEOS.	9 $L.m^{-2}.h^{-1}$ (LMH)	9%, 2000 ppm NaCl, 600 kPa, RO	This study
ENM: Polyvinylidene fluoride (PVDF) TFNC	Polydopamine (PDA)	None.	43 LMH	>97%, 0.5M NaCl, osmotic pressure, Forward osmosis (FO)	[58]
ENM: Polyacrylonitrile (PAN)	Carbon nanotubes (CNTs)	None.	49.2 LMH	7.2 g /m^2h, 1M NaCl, osmotic pressure, FO	[59]
Commercial nylon membrane filter	GO, non TFNC membrane	Aromatic crosslinker, α,α/-dichloro-p-xylene.	11 LMH	50%, 500 mg/L NaCl, 5 bar, Nanofiltration (NF)	[60]
Commercial membrane	GO/MoS_2	sodium alginate/$CaCl_2$.	112.5 LMH	99% dyes, NF	[45]
Commercial polysthersulfone membrane	GO/MoS_2	None.	8 LMH	80%, up to 414 kPa, 50 Mm Na_2SO_4, filtration type not specified	[28]
Commercial cellulose acetate membrane	GO/MoS_2	None. van der Waals forces between GO and MoS_2. Compact interlayer spacing by intercalated MoS2 prevents swelling	48.27 LMH	56%, 1000 ppmNaCl, $K_3Fe(CN)_6$, NF	[43]
ENM: PAN	GO	Chitosan. Varying the pressure allows the hydrated chitosan to adjust the d-spacing when compressed	37 LMH	51.8%, 1.0 g/L Na_2SO_4, 800 kPa, NF	[61]

Future work:

Possibility of membrane reusability: the high stability of the prepared rPET-GO/MoS_2 may also be highly beneficial to the membrane reusability for a few cycles. In addition, good membrane hydrophilicity and the antifouling properties of MoS_2 is also one of the features affording it for longevity and robustness

Up-scaling: conducting desalination experiments using real sea water containing complex ions and organic matter, and running the tests using larger experimental set-up, as well as at prolonged periods of 24 to 48 hours. In addition, the use of much higher pressures and investigating the effect of pressure on the d-spacing of the membrane.

The electrospinning of rPET and the vacuum-assisted filtration (VASA) for interlayer deposition are both scalable techniques. Roll-to-roll electrospinning is an established industrial process. The VASA step, while batch-based, can be scaled to larger membrane areas. The main challenge for industrial desalination would be reinforcing the ENM to withstand high pressures (>15 bar), potentially by adding a non-woven fabric support layer or by hybrid electrospinning/electrospraying.

Strategies to further improve the GO/MoS_2 coating layer: Synthesizing MoS_2 in the presence of GO to promote more intimate mixing and covalent bonding, potentially leading to even better film formation and stability. Furthermore, exploring other alternative synthesis routes, such as the in-situ growth of MoS_2 on GO nanosheets, in attempt to enhance intermixing and interfacial bonding. In addition, further elemental mapping techniques such as EDX should be employed to conclusively confirm the distribution and interaction of MoS2 within the GO layers.

Further characterizations: Pore size measurements for all the membranes after modification using appropriate techniques such as the Capillary Flow Porometry or Liquid-Liquid Displacement Porometry for the non-porous PA deposited membrane, and AFM for GO and GO/MoS_2 membranes

4. Conclusion

The main objective of the study was to develop electrospun nanofibrous membranes (ENMs) fit for desalination, which function as support layers to the active layer of the thin film nanocomposite (TFNC) membranes. The highly porous ENM with interconnected pore structure was intended to replace the conventional phase inverted substrates that comprise the dead-end pores (i.e., nonporous), to alleviate the low flux rates of the current thin film desalination membranes. rPET was the selected polymer, but owing to its hydrophobicity, it was modified with GO as a hydrophilic nanomaterial. The electrospun rPET substrate was therefore modified by the inclusion of the interlayer to enhance its surface properties (i.e. smoothness and hydrophilicity). This, like the current phase inverted membranes, provided a platform more suited to the formation of the active layer onto the substrate. Coating of GO

sheets onto the microporous electrospun rPET nanofibrous substrate formed a uniform and intact film layer of well-stacked GO layers, to function as an interlayer between the active PA layer and the rPET substrate. The GO interlayer was further modified with the MoS_2 for stability and PVA as a connector to the GO sheets. The MoS_2 successfully intercalated within the GO sheets to control the GO interlayer spacing (which functions as nanochannels for water molecule transport and salt ion rejection). The XRD supplied the evidence of successful intercalation of MoS_2 within the GO sheets thus resulting in the tightening of the interlayer space within the sheets of the rPET-GO/MoS_2 membranes. As the hydrated Na^+ and Cl^- ions are of sizes of 0.72 and 0.66 nm respectively, the obtained nanochannel spacing of the rPET-GO/MoS_2 membranes can be as low as 0.64 nm, and therefore capable of retaining the salt ions. The electrospun rPET as a substrate to the dense nonporous PA active layer facilitated the high permeation of water molecules when compared to the commercially available phase inverted substrates. The GO/MoS_2 interlayer with the tight nanochannels also aided in the retention of salt ions, with the possibility of retaining more salt ions as possible at high pressures. The low fluxes of the current desalination membranes can thus, be overcome. Smooth hydrophilic surfaces are highly preferred for active layer formation. The interlayer, therefore, served as a modification of the highly porous hydrophobic substrate, thus improving the surface roughness, and reducing the pore sizes of the rPET substrate.

Acknowledgments

The authors acknowledge the Department of Science and Innovation (HGERA8X), the Council for Scientific and Industrial Research, CSIR (HGER74P), and the University of Johannesburg (86310), for the financial support. Furthermore, thanks are extended to CSIR, Tshwane University of Technology and the University of South Africa for providing laboratory space and academic assistance. Special appreciation is also given to Ms. Sharon Eggers and Dr. Thomas Malwela for their support with Atomic Force Microscopy.

Data availability statement

Data can be shared upon request. The data that support the findings of this study are available upon reasonable request from the authors

Conflict of interest

The author declares no conflict of interest.

References

[1] H.D. Beyene ,T.G. Ambaye, Application of sustainable nanocomposites for water purification process, Sustainable polymer composites and nanocomposites (2019) 387-412.

[2] T.A. Saleh, Materials, nanomaterials, nanocomposites, and methods used for the treatment and removal of hazardous pollutants from wastewater: Treatment technologies for water recycling and sustainability, Nano-Structures & Nano-Objects 39 (2024) 101231. https://doi.org/10.1016/j.nanoso.2024.101231

[3] O.R. Opetubo, R. Kitalu, P.O. Oviroh, S.T. Oyinbo, P.E. Imoisili, T.-C. Jen, A mini-review on MoS_2 membrane for water desalination: Recent development and challenges, Nanotechnology Reviews 12 (2023). doi:10.1515/ntrev-2022-0563

[4] I. Ndiaye, I. Chaoui, J. Eddouibi, S. Vaudreuil, T. Bounahmidi, Synthesis of poly (vinylidene fluoride)/polyacrylonitrile electrospun substrate-based thin-film composite membranes for desalination by forward osmosis process, Chemical Engineering and Processing - Process Intensification 181 (2022) 109132. https://doi.org/10.1016/j.cep.2022.109132

[5] W. Wu, L. Yu, L. Li, Z. Li, J. Kang, S. Pu, D. Chen, R. Ma, K. An, G. Liu, Electrospun nanofiber based forward osmosis membrane using graphene oxide as substrate modifier for enhanced water flux and rejection performance, Desalination 518 (2021) 115283.

[6] F. Liu, L. Wang, D. Li, Q. Liu, B. Deng, Preparation and characterization of novel thin film composite nanofiltration membrane with pvdf tree-like nanofiber membrane as composite scaffold, Materials & Design 196 (2020) 109101. https://doi.org/10.1016/j.matdes.2020.109101

[7] M. Moslehi, H. Mahdavi, A. Ghaffari, Preparation and characterization of polyamide thin film composite nanofiltration membrane based on polyurethane nanofibrous support, Journal of Polymers and the Environment 29 (2021) 2463-2477. 10.1007/s10924-021-02060-2

[8] H. Mahdavi ,M. Moslehi, A new thin film composite nanofiltration membrane based on pet nanofiber support and polyamide top layer: Preparation and characterization, Journal of Polymer Research 23 (2016) 257. 10.1007/s10965-016-1157-4

[9] N.A.S. Suhaimi, F. Muhamad, N.A. Abd Razak, E. Zeimaran, Recycling of polyethylene terephthalate wastes: A review of technologies, routes, and applications, Polymer Engineering & Science 62 (2022) 2355-2375. https://doi.org/10.1002/pen.26017

[10] T.H. Lin, L.N. Phat, P.M. Tu, T.Q. Thang, B.D.D. Khoa, C.V. Lam, P.T.T. Vy, M.T. Phong, N.H. Hieu, Recycled polyethylene terephthalate fibers aerogels modified with graphene oxide for adsorption of methylene blue and coated with polydimethylsiloxane tetraethyl orthosilicate for oil removal, Journal of Polymers and the Environment 31 (2023) 648-663.

[11] W. Zhang, H. Xu, F. Xie, X. Ma, B. Niu, M. Chen, H. Zhang, Y. Zhang, D. Long, General synthesis of ultrafine metal oxide/reduced graphene oxide nanocomposites for ultrahigh-flux nanofiltration membrane, Nature Communications 13 (2022) 471.

[12] S. Wang, R. Yi, Y. Huang, H. Zuo, Y. Zhang, Y. Huang, L. Chen, S. Liang, “Ion-cage” structure of graphene oxide membranes with stable interlayer spacings towards efficient desalination, Separation and Purification Technology 336 (2024) 126296. https://doi.org/10.1016/j.seppur.2024.126296

[13] F.-x. Kong, Z.-Y. Yang, L.-P. Yue, J.-f. Chen, C.-m. Guo, Nanofiltration membrane with substrate incorporated amine-functionalized graphene oxide for enhanced petrochemical wastewater and shale gas produced water desalination, Desalination 517 (2021) 115246. https://doi.org/10.1016/j.desal.2021.115246

[14] C. Cheng, L. Shen, X. Yu, Y. Yang, X. Li, X. Wang, Robust construction of a graphene oxide barrier layer on a nanofibrous substrate assisted by the

flexible poly (vinylalcohol) for efficient pervaporation desalination, Journal of materials chemistry A 5 (2017) 3558-3568.

[15] S. Zheng, Q. Tu, J.J. Urban, S. Li, B. Mi, Swelling of graphene oxide membranes in aqueous solution: Characterization of interlayer spacing and insight into water transport mechanisms, ACS Nano 11 (2017) 6440-6450. 10.1021/acsnano.7b02999

[16] A.M. Shawky, Y.H. Kotp, M.A. Mousa, M.M.S. Aboelfadl, E.E. Hekal, K. Zakaria, Effect of titanium oxide/reduced graphene (TiO_2/rGO) addition onto water flux and reverse salt diffusion thin-film nanocomposite forward osmosis membranes, Environmental Science and Pollution Research 31 (2024) 24584-24598. 10.1007/s11356-024-32500-0

[17] B. Yuan, M. Wang, B. Wang, F. Yang, X. Quan, C.Y. Tang, Y. Dong, Cross-linked graphene oxide framework membranes with robust nano-channels for enhanced sieving ability, Environmental Science & Technology 54 (2020) 15442-15453. 10.1021/acs.est.0c05387

[18] C. Cheng, L. Shen, X. Yu, Y. Yang, X. Li, X. Wang, Robust construction of a graphene oxide barrier layer on a nanofibrous substrate assisted by the flexible poly(vinylalcohol) for efficient pervaporation desalination, Journal of Materials Chemistry A 5 (2017) 3558-3568. 10.1039/C6TA09443K

[19] M.-W. Sun, Z. Li, Q.-Y. Wang, N. Zhang, R. Xie, X.-J. Ju, W. Wang, Z. Liu, L.-Y. Chu, MoS_2 laminate membranes with structural-phase-dependent permeation for molecular separation, Cell Reports Physical Science 4 (2023). 10.1016/j.xcrp.2022.101239

[20] C. Du, G. Liu, Z. Qu, W. Wang, D. Yu, Go/TiO_2-decorated electrospun polyvinylidene fluoride membrane prepared based on metal-polyphenol coordination network for oil–water separation and desalination, Journal of Materials Science 57 (2022) 3452-3467. 10.1007/s10853-021-06824-y

[21] A. Ishag ,Y. Sun, Recent advances in two-dimensional MoS_2 nanosheets for environmental application, Industrial & Engineering Chemistry Research 60 (2021) 8007-8026. 10.1021/acs.iecr.1c01311

[22] P.O. Oviroh, T.-C. Jen, J. Ren, A. van Duin, Towards the realisation of high permi-selective MoS_2 membrane for water desalination, npj Clean Water 6 (2023) 14. 10.1038/s41545-023-00228-y

[23] N. Meng, X. Sun, J. Liu, J. Mi, R. Rong, Effect of addition amount of ethylenediamine on interlayer nanochannels and the separation performance of graphene oxide membranes, Polymers 16 (2024) 3123.

[24] P. Zhuang, Z. Guo, S. Wang, Q. Zhang, M. Zhang, L. Fu, H. Min, B. Li, K. Zhang, Interfacial hydrothermal assembly of three-dimensional lamellar reduced graphene oxide aerogel membranes for water self-purification, ACS Omega 6 (2021) 30656-30665. 10.1021/acsomega.1c04466

[25] J. Gao, M. Zhang, J. Wang, G. Liu, H. Liu, Y. Jiang, Bioinspired modification of layer-stacked molybdenum disulfide (mos2) membranes for enhanced nanofiltration performance, ACS omega 4 (2019) 4012-4022.

[26] H. Yang, Y. Huang, Y. Zhao, A. Fan, Sensitive chemiluminescent sensing method for mercury (ii) ions based on monolayer molybdenum disulfide, Analytical Sciences 35 (2019) 551-556.

[27] A. Di Bartolomeo, L. Genovese, T. Foller, F. Giubileo, G. Luongo, L. Croin, S.-J. Liang, L. Ang, M. Schleberger, Electrical transport and persistent photoconductivity in monolayer MoS_2 phototransistors, Nanotechnology 28 (2017) 214002.

[28] M. Wang, J.J. Urban, B. Mi, Heterogeneous MoS_2-GO membranes with enhanced resistance to swelling and restacking, Journal of Membrane Science 697 (2024) 122548. https://doi.org/10.1016/j.memsci.2024.122548

[29] E. Hoenig, S.E. Strong, M. Wang, J.M. Radhakrishnan, N.J. Zaluzec, J.L. Skinner, C. Liu, Controlling the structure of MoS_2 membranes via covalent functionalization with molecular spacers, Nano Letters 20 (2020) 7844-7851. 10.1021/acs.nanolett.0c02114

[30] K. Selatile, S.S. Ray, V. Ojijo, R.E. Sadiku, Morphological, thermal, and mechanical properties of electrospun recycled poly (ethylene terephthalate)/graphene oxide composite nanofiber membranes, ACS omega 6 (2021) 21005-21015.

[31] N. Kumar, K. Setshedi, M. Masukume, S.S. Ray, Facile scalable synthesis of graphene oxide and reduced graphene oxide: Comparative investigation of different reduction methods, Carbon Letters 32 (2022) 1031-1046. 10.1007/s42823-022-00335-9

[32] N. Kumar, E. Fosso-Kankeu, S.S. Ray, Achieving controllable mos2 nanostructures with increased interlayer spacing for efficient removal of Pb(ii) from aquatic systems, ACS Applied Materials & Interfaces 11 (2019) 19141-19155. 10.1021/acsami.9b03853

[33] K. Selatile, S.S. Ray, V. Ojijo, R.E. Sadiku, Morphological, thermal, and mechanical properties of electrospun recycled poly(ethylene terephthalate)/graphene oxide composite nanofiber membranes, ACS Omega 6 (2021) 21005-21015. https://doi.org/10.1021/acsomega.1c02578

[34] M.K. Zamisa, S.S. Ray, M.M. Madirisha, V. Ojijo, T. Seadira, R.E. Sadiku, N. Kumar, J. Orasugh, Enhancing water permeability in thin-film nanocomposite membranes utilizing electrospun recycled pet and graphene oxide, Nano Express 6 (2025) 015012. 10.1088/2632-959X/ad9298

[35] M.A. Raza, A. Islam, A. Sabir, N. Gull, I. Ali, R. Mehmood, J. Bae, G. Hassan, M.U. Khan, PVA/TEOS crosslinked membranes incorporating zinc oxide nanoparticles and sodium alginate to improve reverse osmosis performance for desalination, Journal of applied Polymer science 136 (2019) 47559.

[36] Q. Wang, L. Hu, H. Ma, S. Venkateswaran, B.S. Hsiao, High-flux nanofibrous composite reverse osmosis membrane containing interfacial water channels for desalination, ACS Applied Materials & Interfaces 15 (2023) 26199-26214. 10.1021/acsami.2c15509

[37] L. Meng, F. Niu, P. Deng, N. Li, Y. Lv, M. Huang, Electrospun nanofiber supports with bio-inspired modification enabled high-performance forward osmosis composite membranes, Composites Communications 22 (2020) 100473. https://doi.org/10.1016/j.coco.2020.100473

[38] Y.S. Khoo, W.J. Lau, S.W. Hasan, W.N.W. Salleh, A.F. Ismail, New approach of recycling end-of-life reverse osmosis membranes via sonication for microfiltration process, Journal of Environmental Chemical Engineering 9 (2021) 106731. https://doi.org/10.1016/j.jece.2021.106731

[39] S. Yurdakal, C. Garlisi, L. Özcan, M. Bellardita, G. Palmisano, *Chapter 4 - (photo)catalyst characterization techniques: Adsorption isotherms and bet, sem, ftir, uv–vis, photoluminescence, and electrochemical characterizations*, in *Heterogeneous photocatalysis*, G. Marcì and L. Palmisano, Editors. 2019, Elsevier. p. 87-152.

[40] J. Sun, Y. Chen, C. Hu, H. Liu, J. Qu, Modulation of cation trans-membrane transport in GO-MoS_2 membranes through simultaneous control of interlayer

spacing and ion-nanochannel interactions, Chemosphere 222 (2019) 156-164. https://doi.org/10.1016/j.chemosphere.2019.01.129

[41] S. Kim, R. Ou, Y. Hu, X. Li, H. Zhang, G.P. Simon, H. Wang, Non-swelling graphene oxide-polymer nanocomposite membrane for reverse osmosis desalination, Journal of membrane science 562 (2018) 47-55.

[42] S.H. Abebe, T.M. Subrahmanya, H.F.M. Austria, S. Nayak, T.-H. Huang, O. Setiawan, W.-S. Hung, C.-C. Hu, K.-R. Lee, J.-Y. Lai, High performance lamellar structured graphene oxide nanocomposite membranes via Fe_3O_4-coordinated phytic acid control of interlayer spacing for organic solvent nanofiltration (osn), Chemical Engineering Journal 495 (2024) 153451. https://doi.org/10.1016/j.cej.2024.153451

[43] J. Ma, X. Tang, Y. He, Y. Fan, J. Chen, Robust stable MoS_2/GO filtration membrane for effective removal of dyes and salts from water with enhanced permeability, Desalination 480 (2020) 114328.

[44] Q. Lan, C. Feng, Z. Wang, L. Li, Y. Wang, T. Liu, Chemically laminating graphene oxide nanosheets with phenolic nanomeshes for robust membranes with fast desalination, Nano Letters 21 (2021) 8236-8243. 10.1021/acs.nanolett.1c02683

[45] J. Mo, S. Wang, F. Xie, S. Liang, X.-H. Ma, Double cross-linked MoS_2 intercalation GO membrane: Towards high stability and high permeability, Separation and Purification Technology 314 (2023) 123523. https://doi.org/10.1016/j.seppur.2023.123523

[46] M.-N. Li, X.-J. Chen, Z.-H. Wan, S.-G. Wang, X.-F. Sun, Forward osmosis membranes for high-efficiency desalination with nano- MoS_2 composite substrates, Chemosphere 278 (2021) 130341.

[47] A. Darmawan, H. Muhtar, D.N. Pratiwi, M. Elma, Y. Astuti, C. Azmiyawati, Robust construction of polyvinyl alcohol intercalated graphene oxide nanofiltration membrane for desalination via pervaporation, Chemosphere 360 (2024) 142437. https://doi.org/10.1016/j.chemosphere.2024.142437

[48] J. Sun, X. Qian, Z. Wang, F. Zeng, H. Bai, N. Li, Tailoring the microstructure of poly(vinyl alcohol)-intercalated graphene oxide membranes for enhanced desalination performance of high-salinity water by pervaporation, Journal of Membrane Science 599 (2020) 117838. https://doi.org/10.1016/j.memsci.2020.117838

[49] M.S. Islam, K. Touati, M.S. Rahaman, High flux and antifouling thin-film nanocomposite forward osmosis membrane with ingrained silica nanoparticles, ACS ES&T Engineering 1 (2021) 467-477.

[50] M. Huang, L. Meng, B. Li, F. Niu, Y. Lv, Q. Deng, J. Li, Fabrication of innovative forward osmosis membranes via multilayered interfacial polymerization on electrospun nanofibers, Journal of Applied Polymer Science 136 (2019) 47247.

[51] J. Qin, Y. Zhang, S.E. Lowe, L. Jiang, H.Y. Ling, G. Shi, P. Liu, S. Zhang, Y.L. Zhong, H. Zhao, Room temperature production of graphene oxide with thermally labile oxygen functional groups for improved lithium ion battery fabrication and performance, Journal of materials chemistry A 7 (2019) 9646-9655.

[52] F. Najafi ,M. Rajabi, Thermal gravity analysis for the study of stability of graphene oxide–glycine nanocomposites, International Nano Letters 5 (2015) 187-190.

[53] P. Das ,P. Tiwari, Thermal degradation study of waste polyethylene terephthalate (pet) under inert and oxidative environments, Thermochimica Acta 679 (2019) 178340.

[54] Z. Wang, F. He, J. Guo, S. Peng, X.Q. Cheng, Y. Zhang, E. Drioli, A. Figoli, Y. Li, L. Shao, The stability of a graphene oxide (GO) nanofiltration (nf) membrane in an aqueous environment: Progress and challenges, Materials Advances 1 (2020) 554-568.

[55] F. Luo, J. Wang, Z. Yao, L. Zhang, H. Chen, Polydopamine nanoparticles modified nanofiber supported thin film composite membrane with enhanced adhesion strength for forward osmosis, Journal of Membrane Science 618 (2021) 118673.

[56] W. Hirunpinyopas, E. Prestat, S.D. Worrall, S.J. Haigh, R.A. Dryfe, M.A. Bissett, Desalination and nanofiltration through functionalized laminar MoS_2 membranes, *ACS nano* 11 (2017) 11082-11090.

[57] Y. Li, C. Li, S. Li, B. Su, L. Han, B. Mandal, Graphene oxide (GO)-interlayered thin-film nanocomposite (TFN) membranes with high solvent resistance for organic solvent nanofiltration (osn), *J. Mater. Chem. A* 7 (2019) 13315-13330.

[58] B. Li, X.-X. Ke, Z.-H. Yuan, L.-B. Zhong, Q.-B. Zhao, Y.-M. Zheng, High performance electrospun thin-film composite forward osmosis membrane by tailoring polyamide active layer with polydopamine interlayer for desulfulrization wastewater desalination, *Desalination* 534 (2022) 115781. https://doi.org/10.1016/j.desal.2022.115781

[59] Y. Yang, Y. Xu, Z. Liu, H. Huang, X. Fan, Y. Wang, Y. Song, C. Song, Preparation and characterization of high-performance electrospun forward osmosis membrane by introducing a carbon nanotube interlayer, *J. Membr. Sci.* 616 (2020) 118563. https://doi.org/10.1016/j.memsci.2020.118563

[60] H. Kwon, Y. Park, E. Yang, T.-H. Bae, Graphene oxide-based membranes intercalated with an aromatic crosslinker for low-pressure nanofiltration, *Membranes* 12 (2022) 966.

[61] C. Xing, J. Han, X. Pei, Y. Zhang, J. He, R. Huang, S. Li, C. Liu, C. Lai, L. Shen, A.K. Nanjundan, S. Zhang, Tunable graphene oxide nanofiltration membrane for effective dye/salt separation and desalination, *ACS Appl. Mater. Interfaces* 13 (2021) 55339-55348. 10.1021/acsami.1c16141